CD-type discretization for sea ice dynamics in FESOM version 2

Sergey Danilov[1,2], Carolin Mehlmann[3], Dmitry Sidorenko[1], and Qiang Wang[1]

[1]Alfred Wegener Institute, Helmholtz Centre for Polar and Marine Research, Bremerhaven, Germany
[2]Jacobs University, Bremen, Germany
[3]Otto-von-Guericke University, Magdeburg, Germany

Correspondence: sergey.danilov@awi.de

Abstract. Two recently proposed variants of CD-type discretizations of sea-ice dynamics on triangular meshes are implemented in the Finite volumE Sea ice - Ocean Model (FESOM version 2). The implementations employ the finite element method in spherical geometry using longitude-latitude coordinates. Both of them rely on the edge-based sea-ice velocity vectors, but differ in basis functions used to represent velocities. The first one uses nonconforming linear (Crouzeix–Raviart) basis

5   functions, and the second one uses continuous linear basis functions on subtriangles obtained by splitting parent triangles into four smaller triangles. Test simulations are used to show how the performance of the new discretizations compares with the A-grid discretization using linear basis functions. Both the CD discretizations are found to simulate a finer structure of linear kinematic features (LKFs). Only the first CD variant demonstrates some sensitivity to the representation of scalar fields (sea-ice concentration and thickness), simulating a finer structure of LKFs with the cell-based scalars than with the vertex-based

10   scalars.

1 Introduction

The appearance of several global ocean models formulated on unstructured (triangular or hexagonal) meshes, such as FESOM (Wang et al., 2014; Danilov et al., 2017), MPAS-Ocean (Ringler et al., 2013; Petersen et al., 2019) and ICON-O (Korn, 2017) triggered the development of sea-ice models taylored to such meshes. Very recently, the sea-ice component of FESOM

15   (FESIM, Danilov et al. (2015)), MPAS-Ocean (MPAS-Seaice, Turner et al. (2021) and Capodaglio et al. (2022)) and ICON-O (Mehlmann and Korn, 2021; Mehlmann and Gutjahr, 2022) have been documented. FESIM (Danilov et al., 2015) relies on the finite element method and the collocated piece-wise linear $P_1 - P_1$ discretization. In this case the discrete sea-ice velocities and scalar quantities (concentration, thicknesses) are placed at mesh vertices, and the discrete fields are assumed to be linear functions on triangles. This is an example of A-grid discretization, in terminology of Mehlmann et al. (2021). The original

20   formulation of MPAS-Seaice by Turner et al. (2021) follows the B-grid discretization. In this case the discrete sea-ice velocities are placed at the vertices of hexagons and scalars are placed at hexagon centers. This corresponds to the cell (triangle) placement of velocity and the vertex placement of scalars on dual triangular meshes. Several variants of discretization are proposed by Turner et al. (2021), based on either variational principles or the finite volume method. The new MPAS-Seaice variational discretization developed by Capodaglio et al. (2022) places sea-ice velocity vectors at mesh edges. The same staggering is

25   used by Mehlmann and Korn (2021) to discretize the sea-ice module of ICON-O on triangular meshes. The discretization

by Mehlmann and Korn (2021) employs linear nonconforming (Crouzeix–Raviart) finite elements, while the approximation by Capodaglio et al. (2022) uses either Wachspress (Dasgupta (2003)) or piece-wise linear representation on sub-polygons into which the mesh cells are additionally split. The discretizations with velocity located at edges are referred to as CD-grid discretizations (Mehlmann et al., 2021).

30   On triangular meshes, the A, B and CD placement of discrete sea-ice velocity results in different numbers of discrete degrees of freedom (DOF), with a ratio of 1:2:3. The CD placement implies three times more degrees of freedom than the A-grid discretization used by FESOM (Danilov et al. (2015)) and hence finer effective resolution. An elementary Fourier analysis of the accuracy of the discrete stress divergence operator on triangular A, B and CD grids (see Danilov et al. (2022)) also shows that the accuracy correlates with the number of DOF. This is the main motivation for considering CD-type of discretizations for

35   sea-ice dynamics. However, the numerical efficiency, robustness and sea ice lead-resolving capability of a particular placement depends on the implementation details.

     This paper presents the new implementation of two CD-grid discretizations in the sea-ice component of FESOM. Both rely on the standard Hibler viscous-plastic (VP) rheology (Hibler, 1979) and use the modified elastic viscous plastic (mEVP) method (Bouillon et al., 2013; Kimmritz et al., 2015). The first variant, to be referred to further as CD1, follows Mehlmann

40   and Korn (2021), but is formulated in longitude–latitude coordinates. It contains additional metric terms, but does not need to transform velocities between local tangent coordinate systems (Mehlmann and Gutjahr, 2022). This discretization is based on the nonconforming linear (Crouzeix–Raviart) finite elements. These elements need stabilization when applied to problems involving full stress divergence (Falk, 1991). The stabilizing term in sea-ice momentum equation used by Mehlmann and Korn (2021) is similar to the one proposed in Hansbo and Larson (2003). The strength of stabilization is well defined in the case of

45   VP method, but requires adjustments in the case of the mEVP method.

     The second CD-grid discretization, referred to as CD2, is similar to that used by Capodaglio et al. (2022), but differs through a systematic finite-element derivation based on piece-wise linear basis functions defined on sub-triangles obtained by splitting the mesh triangles into four equal smaller triangles, and reconstruction of velocities at vertex locations based on edge velocities. The option of Capodaglio et al. (2022) using the Wachspress basis is not pursued. Some further (not important) differences are

50   due to our use of locally flat triangles.

     We use the test case proposed by Mehlmann et al. (2021) to compare the performance of CD1 and CD2 discretizations and the existing A-grid discretization of FESOM. It fact, the results of FESOM simulations based on CD1 have already been used in Mehlmann et al. (2021), but the description of the implementation in FESOM was missing. Since CD-discretizations use 3 times more discrete velocities than the A-grid, we also compare the performance of CD1 and CD2 discretizations with the

55   performnce of a $\sqrt{3}$ finer A-grid.

     The following sections describe main equations (Section 2), the implementation and the Fourier analysis (Section 3), and test simulations (Secton 4). They are followed by Discussions (Secton 5) and Conclusions (Section 6).

2 Equations of sea ice dynamics

The sea-ice momentum equation is written as

$$m(\partial_t + \mathbf{f}\times)\mathbf{u} = a_{ice}\boldsymbol{\tau} - aC_d\rho_o(\mathbf{u} - \mathbf{u}_o)|\mathbf{u} - \mathbf{u}_o| + \mathbf{F} - mg\nabla H. \tag{1}$$

Here, $m = \rho_{ice}h_{ice} + \rho_s h_s$ is the total mass of ice and snow per unit area, with ρ_{ice} and ρ_s the sea ice and snow densities and h_{ice} and h_s the respective mean thicknesses (volumes per unit area), C_d is the ice-ocean drag coefficient, ρ_o is the water density, a_{ice} is the sea ice concentration, $\mathbf{u} = (u, v)$ and $\mathbf{u}_o$ are the sea ice and ocean velocities, $\boldsymbol{\tau}$ is the wind stress applied to sea ice, H is the sea surface elevation, g is the acceleration due to gravity and $\mathbf{F} = \nabla \cdot \boldsymbol{\sigma}$ is the force from the internal stresses in ice (Hibler, 1979),

$$\boldsymbol{\sigma} = 2\eta\dot{\boldsymbol{\epsilon}} + (\zeta - \eta)\mathsf{I}\mathrm{tr}\dot{\boldsymbol{\epsilon}} - \frac{1}{2}\mathsf{I}P_0\frac{\Delta}{\Delta + \Delta_{min}}, \tag{2}$$

where

$$\dot{\boldsymbol{\epsilon}} = \frac{1}{2}\left(\nabla\mathbf{u} + (\nabla\mathbf{u})^T\right) \tag{3}$$

is the strain rate tensor, η and ζ are the viscosities,

$$\Delta^2 = (\dot{\epsilon}_{11}^2 + \dot{\epsilon}_{22}^2)(1 + e^{-2}) + 4\dot{\epsilon}_{12}^2 e^{-2} + 2\dot{\epsilon}_{11}\dot{\epsilon}_{22}(1 - e^{-2}), \tag{4}$$

I is the identity matrix and P_0 is the ice strength. Here, $\dot{\epsilon}_{11}, \dot{\epsilon}_{12}$ and $\dot{\epsilon}_{22}$ are the components of the symmetric tensor $\dot{\boldsymbol{\epsilon}}$ (3) with respect to the orthogonal basis given by unit zonal (with index 1) and meridional (with index 2) vectors and

$$P_0 = h_{ice}p^*e^{-C(1-a_{ice})}, \quad \zeta = \frac{P_0}{2(\Delta + \Delta_{min})}, \quad \eta = \frac{\zeta}{e^2}. \tag{5}$$

The default parameters are $e = 2$, $C = 20$, $\Delta_{min} = 2\cdot10^{-9}$ s^{-1}, and $p^* = 27500$ N/m^2. Δ_{min} regularizes plastic behavior if Δ is very small, replacing it with a viscous flow. To suppress sea ice motion in the absence of forcing, the last term in (2) contains an additional factor (after P_0), i.e. the replacement pressure (Hibler and Ip, 1995).

The modified elastic viscous plastic method (mEVP) is used to solve for the sea ice dynamics in the same form as in Danilov et al. (2015) and Koldunov et al. (2019b). This method is a reformulation of the original EVP method described by Hunke and Dukowicz (1997), and is preferred here because it removes the association of sub-cycling time step of the standard elastic viscous plastic method with numerical stability (Lemieux et al., 2012; Bouillon et al., 2013; Kimmritz et al., 2015). The stability is governed by additional dimensionless parameters α and β. The product $\alpha\beta$ should be sufficiently large compared to $\pi^2 P_0 \Delta t(\Delta + \Delta_{min})^{-1}m^{-1}\Delta x^{-2}$ (Bouillon et al., 2013; Kimmritz et al., 2015) for numerical stability of the iterative procedure. Even though the number of iterations N_{EVP} should be formally larger than α, β to ensure convergence to VP, it has been demonstrated by, e.g., Kimmritz et al. (2017) and Koldunov et al. (2019b) that much smaller N_{EVP} is often sufficient in practice. Simulations reported below use $N_{EVP} = 100$ and α, β are adjusted to ensure stability for the resolution and discretization used.

3 Discretizations

3.1 Spherical geometry

In the discretization of the sea-ice momentum equation, spherical geometry is taken into account similarly to Danilov et al.
(2015), and is consistent with Turner et al. (2021) and Capodaglio et al. (2022) apart from some modifications due to the
weak formulation in our case and the approximation of locally flat triangles (vs. tangent plane). We use longitude-latitude
coordinates (ϕ, θ). In realistic applications these coordinates are those of a rotated coordinate system with the 'north pole'
displaced to the Greenland. The rotation necessitates the transform of forcing and redefines the Coriolis parameter, but has no
other implication for the numerical method. To simplify the description the rotation of the coordinate system is ignored in the
following. The distances $\Delta x, \Delta y$ on mesh triangles are computed with respect to the first triangle vertex using the value of
cosine at triangle center as $\Delta x = R_e \cos \theta_c \Delta \phi$, $\Delta y = R_e \Delta \theta$. The index c implies that the quantity is related to the cell (i.e.
triangle), and R_e is Earth's radius. These distances are used to compute arrays of vertex or edge weights that define derivatives
in zonal and meridional directions on triangles (see sections 3.2 and 3.3). Additional metric terms appear in computations
of strain rates and in computations of stress divergence. They are specified below. Apart from these additional metric terms
and cosines used in computations of relative distances and derivatives, all other computations look as if the geometry were
flat. Therefore, we use ∂_x and ∂_y to denote spatial derivatives as defined in $\nabla = (\partial_x, \partial_y) = (1/R_e)((1/\cos \theta)\partial_\phi, \partial_\theta)$ and local
Cartesian coordinates on triangles. Under this convention the previously introduced indices 1 and 2 in equation (4) are x and
y. The FESOM simulations described below are carried out using a flat geometry which is achieved by setting the values of
$\cos \theta_c$ to 1 and the metric factor to zero. The cosines and metric factors are stored in arrays which are filled before the time
stepping, so switching between flat and spherical geometries does not affect the code.

3.2 Case CD1: A CD-discretisation based on non-conforming linear finite elements

For brevity, we will begin with the VP momentum equation (1), and then explain the modifications needed for the mEVP
method. The momentum equation is first projected on some sufficiently smooth test functions $\mathbf{w}$. The internal stress is inte-
grated by parts to obtain a weak formulation

$$\int m\mathbf{w} \cdot \partial_t \mathbf{u} dS = \int \mathbf{w} \cdot \mathbf{R} dS - \int \nabla \mathbf{w} : \boldsymbol{\sigma} dS - \int mg\mathbf{w} \cdot \nabla H dS. \tag{6}$$

Here $\mathbf{R}$ combines all other terms except for those that are explicitly written. The sea ice velocity is approximated by a series
in nonconforming (Crouzeix–Raviart) linear basis functions,

$$\mathbf{u}^h = \sum_e \mathbf{u}_e(t) N_e(x, y).$$

Here, the summation is over all mesh edges, and $N_e(x, y)$ is the nonconforming linear basis function. It is equal 1 on edge e
and varies linearly to -1 on the vertex v opposite to edge e. In Fig. 1, $N_{e_1} = 1$ on edge e_1, is 0 at midpoints of edges e_2 and
e_3, -1 at v_1 and similarly on the other triangle opposite to the yellow one. N_e is zero outside two triangles sharing edge e.

Note that the nonconforming basis function coincides with the standard linear function defined on a small triangle formed by connecting mid-edge points and then extended to the primary triangle. For this reason, if the set of triangle edges $\{e_1, e_2, e_3\}$ is ordered so that e_1 is opposite to v_1 of the set of triangle vertices $\{v_1, v_2, v_3\}$, see Fig. 1, the derivatives of N_e can be obtained from the (already available in FESOM sea ice module) derivatives of standard linear basis functions by multiplication with -2. A lumped approximation is used for $\mathbf{R}$,

$$\mathbf{R}^h = \sum_e \mathbf{R}_e N_e.$$

We will further suppress the upper index h used to denote discrete approximations. The components of strain rate tensor are written as

$$\dot{\epsilon}_{11} = \partial_x u - v m_f, \dot{\epsilon}_{22} = \partial_y v, \dot{\epsilon}_{12} = (1/2)(\partial_y u + \partial_x v + u m_f),$$

where $m_f = \tan\theta/R$ is the metric factor. To simplify computations, we approximate metric terms by constants on triangles. The discrete strain rates on triangle c become

$$(\dot{\epsilon}_{11})_c = \sum_{e \in E(c)} (u_e \partial_x N_e - (m_f)_c v_e/3), \tag{7}$$

$$(\dot{\epsilon}_{22})_c = \sum_{e \in E(c)} v_e \partial_y N_e, \tag{8}$$

$$(\dot{\epsilon}_{12})_c = (1/2) \sum_{e \in E(c)} (u_e \partial_y N_e + v_e \partial_x N_e + (m_f)_c u_e/3). \tag{9}$$

They are are constant on triangles. Here, $E(c)$ is the set of edges of triangle c.

The stresses are also considered to be constant on triangles, which requires that the ice strength P_0 is constant too. If the scalar degrees of freedom are placed on cells, which is one option in our implementation, the discrete P_0 is constant on triangles without additional approximations. If scalar fields are linear on triangles with the discrete degrees of freedom on vertices, as in Danilov et al. (2015), which is the second option here, P_0 is computed at the central quadrature point, i.e. using mean a_{ice} and h_{ice} on triangle.

The next step is to obtain the Galerkin approximation. The above polynomial approximations are inserted in (6), and the test function is taken as $\mathbf{w} = \mathbf{N}_j = \mathbf{w}_j N_j$, where j is the edge index, and $\mathbf{w}_j$ is an arbitrary weight vector. The equations for sea ice velocity are obtained by requiring that the result holds for any $\mathbf{w}_j$. However, since the nonconforming function $N_e(x, y)$ is discontinuous at edges other than e (except for mid-points), one restricts the integration to triangle interiors and adds penalty (stabilization) terms that effectively connect the triangles:

$$\sum_{c, e \in E(c)} \int_c (m\mathbf{N}_j \cdot \partial_t \mathbf{u}_e N_e - \mathbf{N}_j \cdot \mathbf{R}_e N_e + \nabla \mathbf{N}_j : \boldsymbol{\sigma}_c + mg\mathbf{N}_j \cdot \nabla H) dS_c + S_j = 0. \tag{10}$$

As shown by Hansbo and Larson (2003) (see also Mehlmann and Korn (2021)), the stabilization term is

$$S_j = \sum_e (2C\zeta_e/l_e) \int \int_e [\mathbf{u}] \cdot [\mathbf{N}_j] dl,$$

with C an order one constant, l_e the length of edge e, $[q]$ the jump of quantity q across the edge, and ζ_e the estimate of viscosity ζ on edge e, which is taken as mean over triangles sharing e.

130   The nonconforming functions are orthogonal on elements, so $\int_c N_j N_e dS_c = \delta_{je} S_c/3$, for $j, e \in E(c)$ and zero otherwise. The edge value of mass is obtained as half sum of two nodal or two cell values depending on the discretization of scalar fields. The computations of the third and fourth terms on the left hand side of equation (10) are similar to the computations in Danilov et al. (2015), but we repeat them here for completeness. In spherical geometry, there are metric terms in $\nabla \mathbf{N}_j$, leading to

$$\int_c (\nabla \mathbf{N}_j)_c : \boldsymbol{\sigma}_c dS_c = S_c \mathbf{w}_j \cdot ((\sigma_{11})_c \partial_x N_j + (\sigma_{12})_c \partial_y N_j + (\sigma_{12} m_f)_c/3, (\sigma_{12})_c \partial_x N_j + (\sigma_{22})_c \partial_y N_j - (\sigma_{11} m_f)_c/3). \quad (11)$$

135   The metric contributions initially contained N_j, which left $S_c/3$ after integration over the cell area. Note that compared to the case when the stresses are differenced directly, some metric terms are absent in the weak formulation. The reason is that they originate from differentiation of $\cos\theta$ which is hidden in dS_c in (11). Even if we used a linear representation for $\cos\theta$ on triangle c, the result would be the mean cosine on triangle (absorbed in S_c on the rhs of (11)) because stresses are constant on triangles for linear basis functions.

140   Computations of ∇H in the fourth term on the rhs of (10) do not involve differentiation of metrics. In FESOM, H is known at vertices. The mass at edge j, as above, is the mean of two vertex values for the vertex-based scalars, and two cell values for the cell-based scalars. The result is

$$\int_c mg\nabla H \mathbf{N}_j dS_c = gm_j(S_c/3)\mathbf{w}_j \cdot \nabla H, \quad (12)$$

where $\nabla H = \sum_{v \in V(c)} H_v \nabla M_v$, with M_v the standard linear basis function on triangle c, and $V(c)$ the set of vertices of
145   triangle c.

The integration over edges in the stabilization term involves $\int_e (2l/l_e - 1)^2 dl = l_e/3$, so that l_e drops out of the final result. The stabilization term is computed through two cycles over triangles, similar to Mehlmann and Korn (2021). The first cycle collects the contributions from velocity on the triangle into edge velocity differences, and the second one adds these contributions into equations for edge j. The presence of the stabilization term is critical, as shown by the elementary Fourier analysis
150   (Danilov et al., 2022), there is no approximation for the eigenvalues of discrete divergence of stresses if it is absent.

The extension of this discretization to the mEVP method requires substantial adjustment of the strength of stabilization. The point is that stresses in this method are iterative EVP approximations to the VP stresses, and the stabilization pre-factor has to be essentially smoother than $2C\zeta_e$. Instead of $2C\zeta_e$ we take $CP_0 S_e/\Delta t$, where $S_e = (1/3)(S_{c_1} + S_{c_2})$ the area associated with the edge (with c_1 and c_2 the triangles sharing the edge). C is dimensional in this case and is taken as $C = 2.5$ s^2/m^2.
155   Apart from the intention to make stability of iterative process less sensitive to Δt and changes in mesh resolution, the selection is purely empirical. It was tested in the range of resolutions $2 - 8$ km in computations reported in Mehlmann et al. (2021), but may need additional tuning in other situations. A VP implementation can be a safer way to proceed with the stabilization, but it is not pursued in this work as we employ the EVP or mEVP methods in our practical applications.

As mentioned above, both vertex (P_1) and cell representation of scalar fields is supported in FESOM. In the first case we
160   use the FCT-FEM method of Löhner et al. (1987) as described in Danilov et al. (2015) to advect the tracers. Because of the
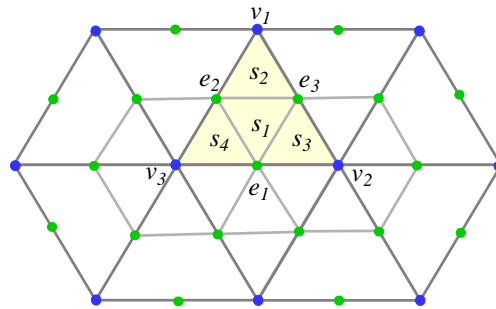
Figure 1. CD1: The nonconforming linear function N_{e_1} on yellow triangle equals 1 on edge e_1, -1 at v_1, and 0 on the line connecting the mid-points of e_2 and e_3. CD2: Triangle c (shaded yellow) is split into four sub-triangles s_1, s_2, s_3 and s_4 by connecting mid-edge points. The set of triangle edges (edge mid-points) $\{e_1, e_2, e_3\}$ is ordered such that they are opposite to triangle vertices $\{v_1, v_2, v_3\}$. The basis function at e_1 is non-zero at the set of sub-triangles that meet at e_1, v_2 or v_3. This basis function equals 1 at e_1, $W_{e_1 v_2}$ at v_2 and $W_{e_1 v_3}$ at v_3, where $W_{e_1 v_2}$ and $W_{e_1 v_2}$ are scalar weights given by (13). It decays linearly to 0 at all other green points of the stencil.

use of consistent mass matrices its high-order part is nominally fourth order in space and second order in time. For the cell-wise constant scalars we use the first-order upwind method, which will be replaced by an FCT method with the second-order high-order part for practical applications in the future.

3.3 Case CD2: A CD-grid dirscretization with conforming linear elements on sub triangles

165 The difference from the previous (CD1) case lies in the selection of basis and test functions. Consider triangle c with vertices $V(c) = \{v_1, v_2, v_3\}$ and edges $E(c) = \{e_1, e_2, e_3\}$, as shown in Fig 1. As mentioned above, the convention is that e_1 is opposite to v_1 and so on. The notation e_1, e_2 and e_3 for edges will be also used to denote the mid-edge points, which should not lead to ambiguities. By connecting the mid-edge points, each primary mesh triangle is split into four smaller triangles. Triangle c in Fig. 1 is split into triangles s_1, s_2, s_3 and s_4 with the following ordering of vertices: $\{e_1, e_2, e_3\}$ for s_1, $\{v_1, e_3, e_2\}$ for

170 s_2, $\{e_3, v_2, e_1\}$ for s_3 and $\{e_2, e_1, v_3\}$ for s_4. The ordering is important, because it allows us to use the array of derivatives computed for the primary triangle. The velocity field is assumed to be linear on each sub-triangle. We store the derivatives of standard linear basis functions M_v, $v \in V(c)$ for each c as matrices G^x_{vc} and G^y_{vc}. The derivatives of linear functions on sub-triangles, by virtue of the ordering described above, are obtained by multiplication of these values with -2 for s_1 and 2 for s_2, s_3 and s_4 for given c. Note that compared to the nonconforming linear basis functions of the previous section, only the

175 representation on sub-triangle s_1 remains the same.

The available degrees of freedom are associated with edge velocities, same as in the previous section, but now the edge velocity is interpreted as a mid-edge value. Values of velocity at mesh vertices are reconstructed as a weighted mean of edge

velocities,

$$\mathbf{u}_v = \sum_{e \in E(v)} W_{ve} \mathbf{u}_e. \tag{13}$$

180 The weights are normalized so as $\sum_{e \in E(v)} W_{ve} = 1$ for each v. They are first taken as inverse of edge lengths, and then normalized. This reconstruction rule and linear representation on sub-triangles imply that for each edge e we are working with a piecewise linear basis function N_e which equals 1 at midpoint of e, goes linearly to 0 at other edge mid-points in triangles sharing e, goes linearly to W_{ve} at the edge vertices, and linearly to 0 at mid-points of other edges joining at vertices. The support of N_{e_1} in Fig. 1 is the combination of sub-triangles meeting at e_1 or v_2 or v_3.

In terms of thus defined N_e, the velocity field is written as

$$\mathbf{u} = \sum_e \mathbf{u}_e N_e.$$

185 In practice, we use two separate arrays, one to store the resolved velocities $\mathbf{u}_e$ and another one to store their vertex reconstructions $\mathbf{u}_v$. Same as for the CD1 discretization, the strain rates are assumed to be constant on sub-triangles, and the metric terms are approximated by constants to achieve this. The ice strength is taken constant on primary triangles, which leads to stresses that are constant on subtriangles. Since there are four sub-triangles in each triangle c, four times more discrete stresses are iterated in the mEVP procedure. This increases computational load compared with the case of nonconforming functions, 190 where the computation cycle is limited to the primary triangles of the mesh.

To obtain the Galerkin approximation, the test function is taken to be any of $\mathbf{N}_j = \mathbf{w}_j N_j$. Since N_j now is continuous, no additional penalty terms are present, in contrast to the CD1 discretization of the previous section, and we get, for edge j

$$\sum_{c,e} \int_c (m \mathbf{N}_j \cdot \partial_t \mathbf{u}_e N_e - \mathbf{N}_j \cdot \mathbf{R}_e N_e + \nabla \mathbf{N}_j : \boldsymbol{\sigma_c} + mg\mathbf{N}_j \cdot \nabla H) dS_c = 0. \tag{14}$$

In the terms with the time derivative and $\mathbf{R}_e$, $\int N_j N_e dS$ are the components of mass matrix. In contrast to the case of nonconforming functions, this matrix is not diagonal now. Similar to Danilov et al. (2015), it is replaced by its diagonally lumped approximation for numerical efficiency,

$$\int N_j N_e dS \approx \delta_{je} S_e,$$

where S_e is the row sum of mass matrix entries. It is equal to

$$S_e = (1/4) \sum_{c \in C(e)} S_c + \sum_{v \in V(e)} W_{ve} S_v,$$

where $S_v = \sum_{c \in C(v)} S_c/12$.

The computations of the third and fourth terms on the left hand side of 14 are done in the double cycle over triangles (external) and sub-triangles (internal). Each term is computed as explained above for the case of nonconforming functions, but now the standard P_1 functions on sub-triangles are used instead of nonconforming functions. The contributions from the stress

divergence from sub-triangles are first collected in an auxiliary edge-based ($\mathbf{F}_e$) and vertex-based ($\mathbf{F}_v$) arrays. For example, the sub-triangle s_2 in Fig. 1 contributes to the edges e_2 and e_3 and to the vertex v_1. On completing the cycle over triangles, the edge-based result $\mathbf{F}_e$ is updated by two vertex based contributions $\mathbf{F}_v$ as

$$\mathbf{F}_e \to \mathbf{F}_e + \sum_{v \in V(e)} W_{ve}\mathbf{F}_v.$$

195 We see that actual basis and test functions N_e are not used in computations. They are, however, needed for the consistent Galerkin formulation, in particular, for defining how to compute S_e. The procedure used by Capodaglio et al. (2022) to determine consistent areas associated with edge degrees of freedom is similar to the one used here, but the finite-element approach automatically determines the areas associated with the computational nodes. Once again, we note that the presence of sub-triangles increases the computational load in finding the stress divergence.

200 3.4 Fourier analysis of CD2

It is instructive to perform the Fourier analysis of CD2. It will provide an independent argument on the accuracy of this discretization, similarly to the analysis in Danilov et al. (2022).

Consider an infinite triangular mesh made of equilateral triangles with side length a and height $h = a\sqrt{3}/2$. Let the axis x be directed along one of the triangle sides, and the y axis along the height drawn to that side. The discrete velocities are located at mid-edges. For the Fourier analysis they are naturally split into three families related to sides with the same orientation. A degree of freedom associated with a particular side of triangle has a neighborhood with the stencil which is oriented differently compared to those associated with other sides. This is why one needs to introduce six (three for u and three for v) separate velocity amplitudes in order to perform the Fourier analysis,

$$\mathbf{u}_e = \mathbf{u}^a e^{i\mathbf{k} \cdot \mathbf{x}_e}, \quad e \in E^a,$$

$$\mathbf{u}_e = \mathbf{u}^b e^{i\mathbf{k} \cdot \mathbf{x}_e}, \quad e \in E^b,$$

$$\mathbf{u}_e = \mathbf{u}^c e^{i\mathbf{k} \cdot \mathbf{x}_e}, \quad e \in E^c$$

Here, the subscript e denotes edges, and E^a, E^b and E^c are the sets containing edges oriented as e_1, e_2 and e_3 (Fig. 1) respectively, $\mathbf{k} = (k, l)$ is the wave vector, and $\mathbf{x}_e$ is the location of mid-edge point of edge e.

A vertex velocity is reconstructed from the edge velocities. The amplitude of vertex velocity is

$$\mathbf{u}^v = (1/3)(\mathbf{u}^a \cos(ka/2) + \mathbf{u}^b \cos(ka/4 + lh/2) + \mathbf{u}^c \cos(-ka/4 + lh/2)).$$

205 The cosines contain phase shifts between a vertex and respective mid-edge points of edges emanating from this vertex.

Same as in Danilov et al. (2022), the stress divergence operator is linearized, the sea-ice strength (and hence the viscosities η and ζ) is taken constant and the geometry is assumed to be flat. One is interested in the eigenvalues of stress divergence operator $\mathsf{V} = \nabla \cdot \boldsymbol{\sigma}$. We take $z = \eta/\zeta = 1$ to ensure that the eigenvalues are sufficiently close to each other in plots.
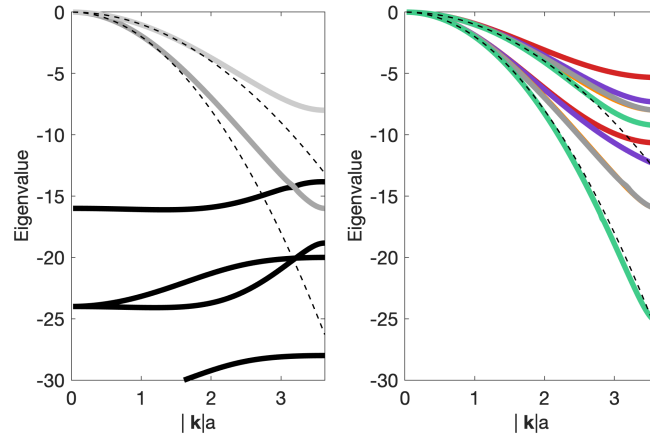
Figure 2. Left panel: The eigenvalues of the (dimensionless) Fourier symbol of $a^2\eta^{-1}\nabla\cdot\boldsymbol{\sigma}$ (thick gray lines) for the discretization CD2 as a function of dimensionless wavenumber $|\mathbf{k}|a$ for the wavevector oriented at $\pi/6$ to the x-axis and $\zeta = \eta$. The thin dashed lines denote the dimensionless eigenvalues $-(k^2 + l^2)a^2$ and $-2(k^2 + l^2)a^2$ of the continuous case. Thick black lines show the spurious branches. Right panel: Comparison with physical eigenvalues of other discretizations (Danilov et al. (2022)). In order of increasing accuracy: A-grid (red), B-grid (Turner et al. (2021), PWL basis) (magenta), CD2 (gray), CD1 (green). B-grid of FESOM is nearly identical to CD2 and is barely seen (orange cast).

We first compute the strain rates on each of the four subtriangles of a primary mesh triangle, see Fig. 1, counting the phases relative to their centers. For example, for subtriangle s_1, formed by the vertices at e_1, e_2 and e_3, the gradients of basis functions on this triangle are $2(0, -1)/h$, $(-\sqrt{3}, 1)/h$ and $(\sqrt{3}, 1)/h$ respectively, so that the amplitude of $\dot{\varepsilon}_{11}$ on this triangle is

$$(\dot{\varepsilon}_{11})_{s_1} = (-\sqrt{3}/h)\mathbf{u}^b e^{-ika/4+ilh/6} + (\sqrt{3}/h)\mathbf{u}^c e^{ika/4+ilh/6},$$

and similarly for all other strain rate components on subtriangle s_1, and also for the strain rates on other subtriangles. Note that
210   the expressions for the gradients and phase shifts depend on the orientation of primary triangles. The expression above is valid for triangles that are oriented as the yellow triangle in Fig. 1. For the primary triangles of opposite orientation (the neighbors of the yellow triangle in Fig. 1) the strain rate amplitudes are minus complex conjugate of the respective results for the triangle (v_1, v_2, v_3). In numerical computations this complication is automatically taken into account when the arrays of derivatives are computed. After the strain rates on subtriangles are computed, the direct stress divergence contributions to edges and vertices
215   are found, and then the edge expressions are updated for vertex contributions, just as done in numerical computations. The resulting Fourier symbol of discrete stress divergence is a 6 by 6 matrix, the eigenvalues of which are found numerically and plotted in the left panel of Fig. 2.

They have to be compared with the eigenvalues of CD1 discretizations given in Danilov et al. (2022). Same as in the case of CD1, there are two physical (thick gray) and four numerical (thick black) branches. The numerical branches are strongly
220   dissipative in the limit of small wavenumbers and do not require any special care. There is no kernel (no zero eigenvalues except for zero wavenumbers), so no stabilization is needed. The right panel of Fig 2 plots the physical eigenvalues found in

Danilov et al. (2022) for other discretizations together with those of CD2 discretization. The range of wavenumbers where the stress divergence eigenvalues give accurate representation of continuous eigenvalues is noticeably narrower for CD2 than for CD1 discretization. We thus expect to see lower resolving power for CD2 compared to CD1. The eigenvalues of CD2 are more
225 accurate than those of the B-grid discretization of Turner et al. (2021) and the A-grid discretization of FESOM. The Fourier analysis only shows that different discretizations have potentially different accuracy. Full nonlinear simulations are needed to judge about their real performance.

4   Comparison of performance

Since this work relies on the already existing discretizations, we only compare the performance of the two new CD methods in
230 FESOM with respect to their numerical efficiency and ability to represent linear kinematic features (LKF) based on the test case proposed by Mehlmann et al. (2021). Their comparison under realistic conditions will be carried out in a separate work. The representation of LKFs is judged qualitatively by their fine structure, and quantitatively, by computing the number of simulated LKFs using the method of Hutter et al. (2019). CD1 and CD2 discretizations are run in two options with the cell-based and vertex-based scalars. One expects that the ability to represent fine structure of LKFs is mainly governed by the number of
235 degrees of freedom used to resolve velocities. However, on triangular meshes, the number of cells is twice that of vertices, which may lead to a more detailed representation of sea ice concentration and thickness. Furthermore, computations of mean ice strength on triangles in our implementations imply averaging for the vertex-based scalars, whereas no averaging is applied in the cell-based case. For more details on the influence of the tracer placement on the resolution of LKFs, see Mehlmann and Danilov (2022). We also compare the CD-grid simulations with those performed with the default A-grid sea-ice discretization
240 of FESOM on a finer mesh with the same number of degrees of freedom as for the CD discretizations.

The test case is run on a triangular mesh occupying a rectangular domain of 512 by 512 km. Except for western and eastern boundaries, the triangles are equilateral. Smaller rectangular triangles are added along the western and eastern boundaries to make the domain exactly rectangular. The side of equilateral triangles is 2 km for CD discretizations. The A-grid simulation is run on the mesh with a triangle side $2/\sqrt{3}$ km. The test case describes the initial phase of sea ice deformation under the
245 forcing of a cyclone moving diagonally to the north-eastern corner. Precise formulation of the test case and forcing parameters can be found in Mehlmann et al. (2021). All simulations use the same external time step $\Delta t = 2$ min. While a larger time step is possible, the selected time step would be typical if the sea-ice model is run together with an ocean model at such spatial resolution. The simulated sea ice patterns at the end of the second day of the model integration are compared. We use $\alpha, \beta = 800$ on A-grid, but increase them to 1500 on CD grids to maintain numerical stability. Our other runs (not shown here)
250 indicate that the sensitivity of the simulations to the precise values of α, β is weak if these values are sufficiently large for stability of the iterative procedure. All runs use $N_{EVP} = 100$, as mentioned earlier.

Figure 3 presents the field of sea ice concentration (left column) and Δ (right column) for CD1 (nonconforming basis functions) in the top row and for CD2 (linear basis functions on sub-triangles) in the bottom row. In both cases the scalars are
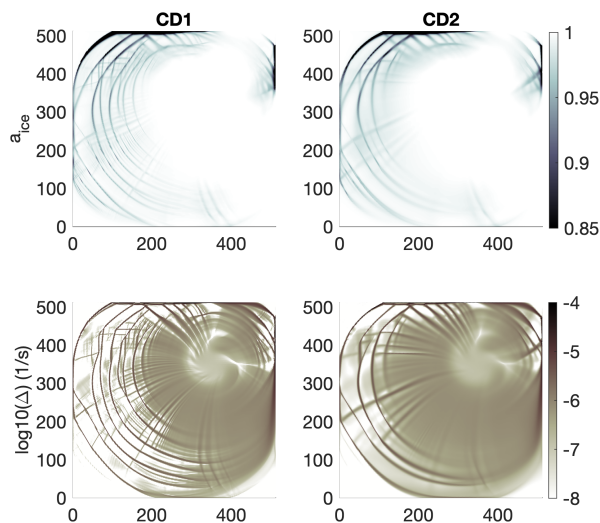
Figure 3. Sea ice concentration (left column) and Δ (right column) in the test case described by Mehlmann et al. (2021), simulated with CD1 discretization (top row) and CD2 discretization (bottom row) with the cell-based sea-ice concentration and thickness.

placed on cells, and the first-order upwind advection is used. It can be seen that the CD1 simulates more LKFs. They are wider
255   and have less small-scale details in CD2.

Figure 4 presents the same fields as Fig. 3 in the first two columns, but for vertex-based scalars. Here too, the ability of CD1 to simulate finer scales is clearly seen in both the concentration and Δ. However, by comparison with the patterns of Fig. 3 we conclude that the vertex placement of scalars leads to some reduction in details in the western parts of the domain for CD1, despite the fact that the high-order advection scheme (see Danilov et al. (2015)) is used in this case in contrast to the highly
260   dissipative first-order upwind scheme used for the cell-based scalars. Averaging vertex sea-ice thickness and concentration to triangles in computations of sea ice strength P_0 for vertex-based scalars may also play a role here. For CD2, almost no difference is seen between the cell and vertex placement. Presumably, because of a lower effective resolution in the momentum part, the presence of smaller scales in scalars does not lead to apparent consequences in contrast to CD1.

The third column in Fig. 4 displays the sea-ice concentration and Δ for the vertex (A-grid) velocity placement but on a finer
265   mesh. The number of velocity degrees of freedom in this case is approximately the same as in the CD cases. Fine scales are better simulated than in the case of CD2, but still less resolved than in the case of CD1. The number of LKFs diagnosed with the algorithm of Hutter et al. (2019) are 114 for the A-grid, and 73 and 75 for CD2 with cell and vertex scalars respectively, to be compared with ≈ 200 for CD1 with cell scalars.
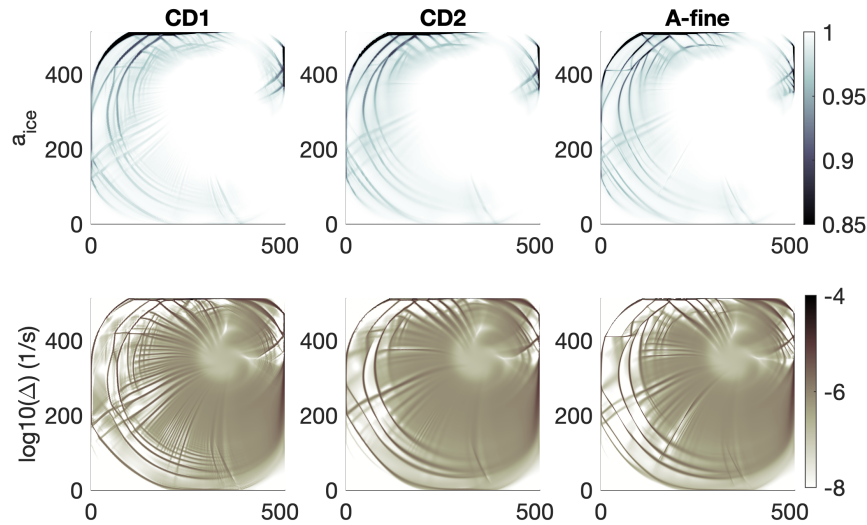
Figure 4. Same as in Fig. 3, but for the cases with vertex-based scalars, for CD1 discretization (the first row), CD2 discretization (the second row) and A-grid discretization (third row). The two CD cases are for a mesh with triangle side of 2 km, while the A-grid case is for a mesh with triangle side of $2/\sqrt{3}$ km.

5 Discussion

270 The higher resolving capability of the CD (edge) placement of velocity compared to the vertex (A-grid) placement is related to its three times larger number of discrete velocities. The larger number of degrees of freedom implies shorter distances between their locations and may potentially lead to a more accurate approximation of differential operators. The gain in accuracy depends on the discretization, and an elementary Fourier analysis of the eigenvalues of the linearized stress divergence operator in Danilov et al. (2022) and in section 3.3 here indicates that CD1 is more accurate than CD2 and both outperform the A-grid

275 discretization. This result agrees with the behaviour of discretizations in the simple test simulations above. We also note that CD1 outperforms A-grid even in terms of LKFs per degree of freedom, as mentioned in Mehlmann and Danilov (2022) and also illustrated above by the A-grid run on a $\sqrt{3}$ times finer mesh.

A caveat of the CD1 discretization is that it needs stabilization to remove kernels in differential operators, as discussed by Mehlmann and Korn (2021). The stabilization constant C requires tuning with the methods of EVP type, and although the

280 empirically found value ensures a reliable work across some tested range of mesh resolutions, it may still need some attention on highly variable meshes. In contrast, CD2 does not require stabilization. From this perspective, it can be viewed as a more robust alternative to CD1.

We also note that CD1 shows a tendency to simulate very close LKFs, separated by several mesh cells. They are well seen in Fig. 3 for cell-based scalars, but become less apparent in Fig. 4 for the vertex-based scalars. It is difficult to judge whether such

285 scales are already affected by numerical errors in full nonlinear case (the accuracy of linear stress divergence operator remains

high for $|\mathbf{k}a| < 2.5$, see Fig. 2). It remains to be seen which of the two CD discretizations on triangular meshes is more reliable in real-world applications on general unstructured meshes.

In our implementation CD1 is approximately two times and CD2 approximately four times more expensive than the A-grid code on the same mesh. In all cases there are two basic cycles over triangles. The stresses are computed in the first cycle and

290 the divergence of stresses is computed in the second cycle. For the A-grid discretization these two cycles take most of CPU time. In CD1, there are two additional cycles over triangles to compute the contribution of stabilization, which largely explains the CPU time doubling. The cycles over triangles in CD2 include an inner cycle over four sub-triangles, which is the main reason for the observed increase in the computational load in this case. We speculate that some optimization is still possible, so these numbers can only be treated as preliminary estimates. In addition to the increase in the time needed for computations,

295 the number of halo exchanges in parallel implementation also increases in the CD cases. As compared to the A-grid code, in our implementation the CD1 discretization requires an additional halo exchange for edge velocity differences. The CD2 case needs additional exchanges for vertex velocities and for the contributions to the divergence of stresses that are assembled at vertices. As demonstrated by Koldunov et al. (2019a), the halo exchanges in sea-ice module is the factor limiting the scalability of FESOM in massively parallel applications. This raises a question on the effect of CD discretizations on scalability, which

300 also requires further work.

The A-grid run on a $\sqrt{3}$ times finer mesh, which ensures the same number of degrees of freedom as in the CD cases, is approximately as computationally expensive as CD2. The fact that it better simulates LKFs than CD2 might be related to much more accurate representation of scalars in this case. However, sea-ice simulations are generally run on the surface mesh of the ocean model, and the potential possibility of using a separate finer mesh for sea ice is not always feasible. One would opt for

305 using CD1 or CD2 instead of A-grid discretization if better resolution of LKFs is required than the one provided by A-grid.

6 Conclusions

We describe implementation of two CD-type discretization of sea-ice mEVP dynamics in FESOM2. They are based on the finite-element method and the use of longitude-latitude coordinates. Both discretizations have been proposed earlier by Mehlmann and Korn (2021) (CD1) and Capodaglio et al. (2022) (CD2), respectively. In the first case, the difference to the

310 original implementation lies in using the longitude-latitude coordinates and the addition of metric terms, which eliminates the need to transform velocities between local tangent coordinate systems. In the second case, the difference lies in using the finite element approach, which makes the derivation more compact and automatically determines the surface area associated with the velocity degree of freedom.

Both CD1 and CD2 demonstrate higher LKF-resolving capability than the A-grid discretization. Although CD2 shows lower

315 resolving capacity than CD1, it may be more robust in (m)EVP dynamics as it does not need much additional adjustment. The new discretizations can be sensitive to particular implementation details. The performance comparison with other available versions of CD1 and CD2 discretization (Mehlmann and Gutjahr (2022), Capodaglio et al. (2022)) will be reported in a

separate work. It also remains to be seen how these new discretizations behave in realistic global climate simulations compared to the standard A-grid discretization of FESOM, which is the subject of our future work.

320 *Code availability.* The exact version of the model used to produce the results used in this paper is archived on Zenodo (Danilov et al., 2023).

Data availability. The mesh files and data files used to draw last two figures are archived together with the code (Danilov et al., 2023).

Author contributions. SD worked on the implementation. All the authors contributed to writing and discussion.

Competing interests. Qiang Wang is a member of the editorial board of Geoscientific Model Development.

Acknowledgements. We acknowledge the use of METIS (Karypis and Kumar (1998)) software package for mesh partitioning and express
325 our thanks to N. Hutter for the use of his LKF diagnostics. This paper is a contribution to the project S2: Improved parameterisations and numerics in climate models of the Collaborative Research Centre TRR 181 "Energy Transfer in Atmosphere and Ocean" funded by the Deutsche Forschungsgemeinschaft (DFG, German Research Foundation) – project no. 274762653. The work of C. Mehlmann is funded by the the Deutsche Forschungsgemeinschaft (DFG, German Research Foundation) - Project number 463061012.

References

330 Bouillon, S., Fichefet, T., Legat, V., and Madec, G.: The elastic-viscous-plastic method revisited, Ocean Modelling, 71, 2–12, 2013.

Capodaglio, G., Petersen, M. R., Turner, A. K., and Roberts, A. F.: An unstructured CD-grid variational formulation for sea ice dynamics, J. Comput. Phys., p. to appear, 2022.

Danilov, S., Wang, Q., Timmermann, R., Iakovlev, N., Sidorenko, D., Kimmritz, M., Jung, T., and Schröter, J.: Finite-element sea ice model (FESIM), version 2, Geoscientific Model Development, 8, 1747–1761, 2015.

335 Danilov, S., Sidorenko, D., Wang, Q., and Jung, T.: The Finite-volumE Sea ice–Ocean Model (FESOM2), Geosci. Model Dev., 10, 765–789, 2017.

Danilov, S., Mehlmann, C., and Fofonova, V.: On discretizing sea-ice dynamics on triangular meshes using vertex, cell or edge velocities, Ocean Modelling, 170, 101 937, https://doi.org/https://doi.org/10.1016/j.ocemod.2021.101937, 2022.

Danilov, S., Mehlmann, C., Sidorenko, D., and Wang, Q.: Sea ice CD-type discretizations of FESOM,
340 https://doi.org/10.5281/zenodo.7646908, 2023.

Dasgupta, G.: Interpolants within convex polygons: Wachspress' shape functions, J. Aerospac. Eng., 16, 1–8, https://doi.org/10.1061/(ASCE)0893-1321(2003)16:1(1), 2003.

Falk, R.: Nonconforming Finite Element Methods for the Equations of Linear Elasticity, Mathematics of Computation, 57, 529–529, 1991.

Hansbo, P. and Larson, M.: Discontinuous Galerkin and the Crouzeix–Raviart element: Application to elasticity, ESAIM, 37, 63–72, 2003.

345 Hibler, III, W. D.: A Dynamic Thermodynamic Sea Ice Model, J. Phys. Oceanogr., 9, 815–846, 1979.

Hibler, III, W. D. and Ip, C. F.: The effect of sea ice rheology on Arctic buoy drift, J. P. Dempsey and Y. D. S. Rajapakse (eds.) ASME AMD, 207, Ice Mechanics, 255–263, 1995.

Hunke, E. C. and Dukowicz, J. K.: An Elastic-Viscous-Plastic model for sea ice dynamics, J. Phys. Oceanogr., 27, 1849–1867, 1997.

Hutter, N., Zampieri, L., and Losch, M.: Leads and ridges in Arctic sea ice from RGPS data and a new tracking algorithm, The Cryosphere,
350 13, 627–645, https://doi.org/10.5194/tc-13-627-2019, 2019.

Karypis, G. and Kumar, V.: A fast and high quality multilevel scheme for partitioning irregular graphs, SIAM Journal on Scientific Computing, 20, 359–392, 1998.

Kimmritz, M., Danilov, S., and Losch, M.: On the convergence of the modified elastic-viscous-plastic method for solving the sea ice momentum equation, J. Comp. Phys., 296, 90–100, 2015.

355 Kimmritz, M., Losch, M., and Danilov, S.: A comparison of viscous-plastic sea ice solvers with and without replacement pressure, Ocean Modelling, 115, 59–69, 2017.

Koldunov, N. V., Aizinger, V., Rakowsky, N., Scholz, P., Sidorenko, D., Danilov, S., and Jung, T.: Scalability and some optimization of the Finite-volumE Sea ice–Ocean Model, Version 2.0 (FESOM2), Geosci. Model Dev., 12, 3991–4012, https://doi.org/https://doi.org/10.5194/gmd-12-3991-2019, 2019a.

360 Koldunov, N. V., Danilov, S., Sidorenko, D., Hutter, N., Losch, M., Goessling, H., Rakowsky, N., Scholz, P., Sein, D., Wang, Q., and Jung, T.: Fast EVP solutions in a high-resolution sea ice model, J. of Advances in Modeling Earth Systems, 11, https://doi.org/https://doi.org/10.1029/2018MS001485, 2019b.

Korn, P.: Formulation of an unstructured grid model for global ocean dynamics, J. Comput. Phys., 339, 525–552, 2017.

Lemieux, J.-F., Knoll, D., Tremblay, B., Holland, D., and Losch, M.: A comparison of the Jacobian-free Newton-Krylov method and the
    EVP model for solving the sea ice momentum equation with a viscous-plastic formulation: a serial algorithm study, J. Comp. Phys., 231,
    5926–5944, 2012.

Löhner, R., Morgan, K., Peraire, J., and Vahdati, M.: Finite-element flux-corrected transport (FEM-FCT) for the Euler and Navier–Stokes
    equations, Int. J. Numer. Methods Fluids, 7, 1093–1109, 1987.

Mehlmann, C. and Danilov, S.: The effect of the tracer staggering on sea ice deformation fields, in: 8th European Congress on Computational
    Methods in Applied Sciences and Engineering, CIMNE, https://doi.org/10.23967/eccomas.2022.267, 2022.

Mehlmann, C. and Gutjahr, O.: Discretization of Sea Ice Dynamics in the Tangent Plane to the Sphere by a CD-Grid-Type Finite Element,
    Journal of Advances in Modeling Earth Systems, 14, e2022MS003 010, 2022.

Mehlmann, C. and Korn, P.: Sea-ice dynamics on triangular grids, J. Comput. Phys., 428, 110 086, 2021.

Mehlmann, C., Danilov, S., Losch, M., Lemieux, J. F., Hutter, N., Richter, T., Blain, P., Hunke, E. C., and Korn, P.: Simulating Linear
    Kinematic Features in Viscous-Plastic Sea Ice models on quadrilateral and triangular Grids With Different Variable Staggering, Journal
    of Advances in Modeling Earth Systems, 13, e2021MS002 523, https://doi.org/https://doi. org/10.1029/2021MS002523, 2021.

Petersen, M. R. A.-D., S., X., Berres, A. S.and Chen, Q., Feige, N., Hoffman, M. J., Jacobsen, D. W., Jones, P. W., Maltrud, M. E., Price,
    S. F., Ringler, T. D., Streletz, G. J., Turner, A. K., Van Roekel, L. P., Veneziani, M., Wolfe, J. D., Wolfram, P. J., and Woodring, J. L.: An
    evaluation of the ocean and sea ice climate of E3SM using MPAS and interannual CORE-II forcing, J. of Advances in Modeling Earth
    Systems, 11, 1438–1458, https://doi.org/https://doi.org/10.1029/2018MS001373, 2019.

Ringler, T., Petersen, M., Higdon, R., Jacobsen, D., Maltrud, M., and Jones, P.: A multi-resolution approach to global ocean modelling,
    Ocean Modell., 69, 211–232, 2013.

Turner, A. K., Lipscomb, W. H., Hunke, E. C., Jacobsen, D. W., Jeffery, N., Engwirda, D., Ringler, T. D., , and Wolfe, J. D.: MPAS-Seaice
    (v1.0.0): Sea-ice dynamics on unstructured Voronoi meshes, Geosci. Mod. Dev., https://doi.org/https://doi.org/10.5194/gmd-2021-355,
    2021.

Wang, Q., Danilov, S., Sidorenko, D., Timmermann, R., Wekerle, C., Wang, X., Jung, T., and Schröter, J.: The Finite Element Sea Ice-Ocean
    Model (FESOM) v. 1.4: formulation of an ocean general circulation model, Geoscientific Model Development, 7, 663–693, 2014.